

What really happens with the electron gas in the famous Franck-Hertz experiment?

F. Sigeneger^{*1}, R. Winkler¹, and R. E. Robson²

¹ Institut für Niedertemperatur-Plasmaphysik, D-17489 Greifswald, Germany

² Research School of Physical Sciences, Australian National University, Canberra, A.C.T. 2600

Received 11 December 2002, revised 17 February 2003, accepted 18 March 2003

Published online 23 July 2003

Key words Field reversal, space-dependent Boltzmann equation, power balance, velocity distribution function

PACS 51.50.+v, 52.25.Dg, 52.25.Fi

The interpretation of the anode current characteristics obtained in the famous Franck-Hertz experiment of 1914 led to the verification of Bohr's predictions of quantised atomic states. This fundamental experiment has been often repeated, and nowadays is generally part of the curriculum in modern physics education. However, the interpretation of the experiment is typically based upon significant simplifying assumptions, some quite unrealistic. This is the case especially in relation to the kinetics of the electron gas, which is in reality quite complex, due mainly to non-uniformities in the electric field, caused by a combination of accelerating and retarding components. This non-uniformity leads to a potential energy valley in which the electrons are trapped. The present state of understanding of such effects, and their influence upon the anode characteristics, is quite unsatisfactory. In this article a rigorous study of a cylindrical Franck-Hertz experiment is presented, using mercury vapour, the aim being to reveal and explain what really happens with the electrons under realistic experimental conditions. In particular, the anode current characteristics are investigated over a range of mercury vapour pressures appropriate to the experiment to clearly elaborate the effects of elastic collisions (ignored in typical discussions) on the power budget, and the trapping of electrons in the potential energy valley.

1 Introduction

The famous Franck-Hertz experiment [1] was developed to verify the existence of quantised energy states in atomic systems and was originally conducted in mercury vapour. Since that time this fundamental experiment and many variants of it [2–5] have been frequently repeated, especially in physics education on modern atomic theory [6, 7] and have been described and qualitatively interpreted in various textbooks on this subject [8, 9].

Apart from the basic features of this experiment with respect to the atomic physics, the kinetics of the electron gas involved is quite complicated. This is particularly so due to the combined effects of accelerating and retarding electric fields, leading to the occurrence of trapped electrons in the region of the extraction grid, and the interplay between elastic and inelastic electron-atom collisions. Generally speaking, considerable simplifications are made for the interpretation and explanation of the behaviour of the electron gas [10, 11] and the resultant anode current characteristics in the experiment. Modelling the real electron velocity distribution by either a mono-energetic beam or a Maxwellian distribution and neglecting the influence of elastic collisions [10] on the electron kinetic properties are particularly problematic assumptions.

A first attempt to model the Franck-Hertz experiment electron kinetics was made recently [11], using a multi-term solution of Boltzmann's equation. Some qualitative features of the experiment, namely spatial oscillations of some transport properties in mercury under the action of a space-independent accelerating field with period length corresponding to the quantised excitation energy, were reproduced. However, the experiment was idealised as taking place without the action of a retarding field in unbounded space, equivalent to a steady-state Townsend experiment, and an approximate method of estimating the anode current was discussed in outline form only.

* Corresponding author: e-mail: sigeneger@inp-greifswald.de, Phone: +49 3834 554 462, Fax: +49 3834 554 301

The present paper rigorously considers many of the details, and indeed goes all the way in modelling actual experiments.

Over the last years considerable progress with respect to the rigorous quantitative analysis of the space-dependent kinetics of the electron gas has been obtained [12, 13]. This analysis includes the effect of nonuniform electric fields on the electron gas as well as the impact of various kinds of electron-atom collision processes. Moreover, very recently the kinetic treatment of trapped electrons [14] has become possible. These recent advances form the basis for the present study of the kinetics of the electron gas arising in the famous Franck-Hertz experiment.

Thus, the main objective of the following presentation is to comprehensively analyse on a kinetic basis the spatial behaviour of the electron gas in the Franck-Hertz experiment conducted in mercury vapour. The analysis is performed in detail for various energy-space averaged, macroscopic electron transport and dissipation properties, for some energy space resolved properties, and, especially, for the resultant anode current characteristics. This study makes it possible, in particular, to quantitatively characterize the velocity distribution of the electrons, the effect of the electron capture and the considerable impact of the energy loss in elastic collisions on the overall power dissipation in the experiment.

Accordingly, the presentation starts with a brief introduction into the model arrangement of the Franck-Hertz experiment and some basic relations of the kinetic treatment.

2 Main aspects of the Franck-Hertz experiment

As in the original work of Franck and Hertz a cylindrical arrangement of the experiment is considered in the following analysis. According to the schematic representation in Fig. 1 the electrons are continuously emitted from the cathode surface at the radius r_c into the region between the cathode and the anode surface at the radius r_a . This region is occupied by mercury atoms of constant density and subdivided by a grid positioned in front of the anode at r_g . Between the cathode and the grid the electron accelerating voltage U_{cg} and between the grid and the anode the electron retarding voltage U_{ga} is applied. Because of the presence of the retarding voltage a certain part of the cathode current is trapped around the grid and extracted from the volume by the grid. Thus, this part cannot contribute to the anode current. This extraction is modelled by a space-dependent electron loss frequency $\nu_g(r)$ that is supposed to act in the immediate vicinity of the grid only.

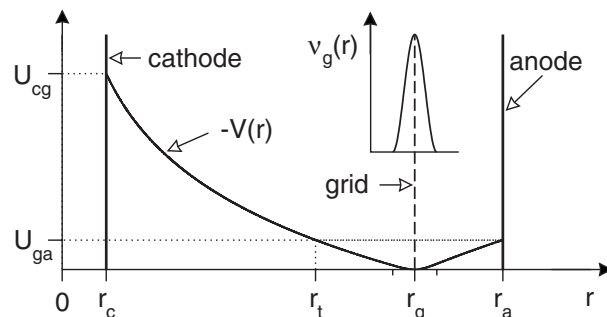


Fig. 1 Schematic setup of the Franck-Hertz experiment.

According to the conventional textbook explanation the physical situation in the steady-state experiment is as follows: Each electron, released from the cathode with almost zero energy by thermionic emission, is accelerated by the voltage between r_c and r_g and thus gains kinetic energy. If its kinetic energy just exceeds the threshold energy of the lowest excitation process of the mercury atoms, the electron suffers an exciting collision and loses largely all its kinetic energy. If this happens close to the grid the electron is trapped by the retarding voltage in front of the anode, can no longer contribute to the anode current and is finally extracted by the grid. Almost the same final state is reached if at higher accelerating voltage the electron can repeatedly undergo exciting collisions on its way and has its last exciting collision close to the grid. However, if the position of the last exciting collision is sufficiently far from the grid the electron can still gain a certain amount of energy on its remaining way to the grid position, can consequently overcome the retarding voltage in front of the anode and contribute further on to

the anode current. Thus, at appropriately fixed retarding voltage U_{ga} the anode current becomes an oscillating function of the applied cathode-grid voltage U_{cg} and the respective cathode-grid voltages related to the maxima of the anode current should be a direct measure of the threshold energy of the lowest inelastic electron-mercury atom collision process.

However, as detailed below the real kinetics of the electrons in the experiment is much more complex than in this conventional picture. There are various points that have a considerable impact on the kinetics of the electrons and consequently on the finally resultant anode current characteristics obtained at fixed retarding voltage U_{ga} . First of all the impact of the energy loss in elastic collisions, in addition to the loss in exciting collisions and the considerable nonuniform energy transport are to be mentioned. Furthermore, the electrons released from the cathode by thermionic emission (i) possess a certain spread of their velocity distribution, (ii) undergo at least two largely overlapping excitation processes with very adjacent threshold energies and (iii) experience a considerable control with respect to the importance of the different energy dissipation channels in collisions by means of the magnitude of the applied cathode-grid voltage U_{cg} and the resultant spatial dependence of the accelerating part of the potential $V(r)$. The usual text book explanations avoid any mention of a distribution of velocities, effectively treating the electrons as a mono-energetic beam, and also neglect elastic collision effects. As McMahon points out [4], the experiment is sometimes misunderstood for these and other reasons.

3 Basic relations of the kinetic study and the boundary conditions

In the cylindrically symmetric and axially uniform arrangement of the Franck-Hertz experiment the spatial evolution of the electron gas is predominantly controlled by the effect of the nonuniform radial electric field $\vec{E}(r) = E(r) \vec{e}_r$, the impact of elastic and inelastic electron-atom collisions and the electron extraction around the grid with the loss frequency $\nu_g(r)$. The electrons are primarily described by their velocity distribution $F(\vec{v}, r)$ which ultimately can be found by solving the corresponding version of the electron Boltzmann equation

$$\vec{v} \cdot \nabla_{\vec{x}} F - \frac{e_0}{m_e} \vec{E} \cdot \nabla_{\vec{v}} F = C^{el}(F) + \sum_l C_l^{in}(F) - \nu_g F. \quad (1)$$

Here $-e_0$ and m_e are the charge and mass of the electron and $C^{el}(F)$ and $C_l^{in}(F)$ denote the collision integrals for elastic collisions and important inelastic collision processes of the electrons with the ground state mercury atoms. Because of the relatively low magnitude of the reduced electric field $E(r)/N$ typically used in the experiment, ionisation is negligible and only elastic and exciting collisions of the electrons with the mercury atoms are of importance in the kinetic study. To simplify the solution of the kinetic equation (1) for the axially uniform cylindrical geometry, a spherical harmonic expansion of the velocity distribution $F(\vec{v}, r)$ with respect to the velocity directions \vec{v}/v has been used in the kinetic equation to derive an appropriate hierarchy equation system [15, 16] for the coefficients of the spherical harmonic expansion. However, when considering the parameter range of the intended application to the experiment in mercury and when taking into account the specific findings of preceding multi-term analyses in mercury [11, 17], it is only necessary to retain the first two terms of the expansion, i.e., to treat the problem in the so-called two term approximation. In this way sufficiently accurate macroscopic as well as energy space resolved properties of the electron gas with remaining inaccuracies of less than few percent can be obtained.

Thus, with the truncated expansion

$$F\left(v, \frac{v_r}{v}, r\right) = \frac{1}{2\pi} \left(\frac{m_e}{2}\right)^{3/2} \left(\bar{f}_0(U, r) + \bar{f}_r(U, r) \frac{v_r}{v}\right), \quad U = \frac{m_e}{2} v^2, \quad v = |\vec{v}| \quad (2)$$

the two coupled equations

$$\begin{aligned} \frac{1}{r} \frac{\partial}{\partial r} \left(r \frac{U}{3} \bar{f}_r \right) - e_0 E(r) \frac{\partial}{\partial U} \left(\frac{U}{3} \bar{f}_r \right) - \frac{\partial}{\partial U} \left(2 \frac{m_e}{M} U^2 N Q^d(U) \bar{f}_0 \right) + \sum_l U N Q_l^{in}(U) \bar{f}_0 \\ - \sum_l (U + U_l^{in}) N Q_l^{in}(U + U_l^{in}) \bar{f}_0(U + U_l^{in}, r) + \nu_g(r) \sqrt{\frac{m_e U}{2}} \bar{f}_0 = 0, \end{aligned} \quad (3)$$

$$U \frac{\partial}{\partial r} \bar{f}_0 - e_0 E(r) U \frac{\partial}{\partial U} \bar{f}_0 + U \left(N Q^d(U) + \sum_l N Q_l^{in}(U) \right) \bar{f}_r + \nu_g(r) \sqrt{\frac{m_e U}{2}} \bar{f}_r = 0 \quad (4)$$

are obtained for the two expansion coefficients $\bar{f}_0(U, r)$ and $\bar{f}_r(U, r)$, with U being the kinetic energy. Furthermore, M , N , $Q^d(U)$, $Q_l^{in}(U)$ and U_l^{in} are the mass and density of the gas atoms, the momentum transfer cross section for elastic collisions, the total cross section and the associated threshold energy of the l th excitation process.

To study the spatial evolution of the electron kinetics in the Franck-Hertz experiment, the system of partial differential equations (3) and (4) for the isotropic distribution $\bar{f}_0(U, r)$ and the anisotropic distribution part $\bar{f}_r(U, r)$ has to be solved in the spatial range between the cathode at r_c and the anode at r_a and for kinetic energies U between 0 and a sufficiently large value U_∞ . The value U_∞ is chosen in such a manner that the overall decrease of the velocity distribution with the energy reaches about ten orders of magnitude, i.e., the distribution becomes negligibly small. Appropriate boundary conditions have to be imposed on both sides of the spatial range as well as of the energy range.

Because of the very frequent elastic electron collisions with the mercury atoms it can be assumed that the electrons released from the cathode by thermionic emission undergo a strong angular scattering immediately in front of the cathode. This conclusion is directly supported by the representation of the mean free path λ^{el} of the elastic collisions in mercury given below in Fig. 2b for the specific experimental conditions. Thus, the energy distribution of the emitted electrons $f_{em}(U)$ largely equals the energy distribution, i.e., the square root of the energy times the isotropic distribution, close to the cathode surface and the appropriate boundary condition at the cathode for $0 \leq U \leq U_\infty$ is

$$\bar{f}_0(U, r_c) = f_{em}(U)/U^{1/2}. \quad (5)$$

The energy distribution of the emitted electrons $f_{em}(U)$ can be approximated by the expression [18]

$$f_{em}(U) = n(r_c) c U \exp\left(-\frac{U}{kT}\right), \quad c = \left(\int_0^\infty U \exp\left(-\frac{U}{kT}\right) dU\right)^{-1}, \quad (6)$$

where $n(r_c)$ is the electron density at the cathode and T is the absolute temperature of the thermionic cathode.

Within the framework of the two term approximation, the boundary condition of the kinetic problem at the anode for $0 \leq U \leq U_\infty$ has been fixed by the relation [19–21]

$$\bar{f}_r(U, r_a) = \frac{3}{2} \frac{1 - \varrho}{1 + \varrho} \bar{f}_0(U, r_a) \quad (7)$$

between \bar{f}_r and \bar{f}_0 describing the partial reflection of the electrons at the anode with reflection coefficient ϱ , whose values lie between zero and unity.

With respect to the energy space appropriate conditions at vanishing and sufficiently large kinetic energy are required. Here the conditions

$$\bar{f}_r(U = 0, r) = 0, \quad (8)$$

$$\bar{f}_0(U \geq U_\infty, r) = 0 \quad (9)$$

for $r_c \leq r \leq r_a$ are used to complete the kinetic problem. These conditions simply state that the anisotropic part \bar{f}_r of the velocity distribution naturally vanishes at zero kinetic energy and that the isotropic part \bar{f}_0 (or the energy distribution) becomes sufficiently small above an appropriately chosen large energy U_∞ .

A further structural simplification of the equation system (3), (4) can be reached if the kinetic energy U is replaced by the total energy ε defined by the relation $\varepsilon = U + W(r)$, where $W(r) = e_0 \int_{r_g}^r E(\tilde{r}) d\tilde{r}$ is the potential energy of the electrons in the electric field $E(r)$ related to the grid position r_g . After the transformation of the equations (3), (4) and of the conditions (5) to (9) to the variable ε a parabolic differential equation problem in ε and r for the transformed distributions $f_i(\varepsilon, r) = \bar{f}_i(U_{\varepsilon r}, r)$ with $i = 0, r$ and $U_{\varepsilon r} = \varepsilon - W(r)$ is obtained. Since ε presents the progression direction of this parabolic problem, it can be efficiently solved as initial-boundary value problem downwards from high to low total energies ε starting with the correspondingly transformed initial condition (9) [22, 23].

The typical shape of the potential $V(r)$ and thus of the potential energy $W(r) = -e_0 V(r)$ occurring in the cylindrical Franck-Hertz experiment is shown in Fig. 1. Thus, the relevant solution area of the kinetic problem in the (ε, r) -space is that above the potential curve $-V(r)$, i.e., $\varepsilon \geq W(r)$, and between the cathode and the

anode. Because of the presence of an accelerating and a retarding potential branch the region $r_t \leq r \leq r_a$ of trapped electrons occurs whose extent depends on both the cathode-grid voltage U_{cg} and the grid-anode voltage U_{ga} . The resultant non-monotonic shape of the potential $-V(r)$ leads to a peculiarity in the solution process in the sense that the solution area in radial direction becomes bounded finally on both sides by the potential profile only where the condition (8) of vanishing anisotropic distribution \bar{f}_r applies.

The numerical solution of the initial-boundary value problem can, after some generalizations and adaptation, ultimately be obtained by a specific solution technique of the parabolic problem that has been detailed and used in former kinetic studies [22, 23].

4 Atomic data and input data of the kinetic approach

For the description of the electron collision processes with mercury atoms a set of reliable as possible collision cross sections is required for energies up to about 10 eV. The Fig. 2a shows the momentum transfer cross section Q^d and the total cross sections Q_l^{in} for the lowest four excitation processes, i.e., that leading to the excitation of the 6^3P_0 , 6^3P_1 , 6^3P_2 and 6^1P_1 state with the corresponding threshold energies 4.67, 4.89, 5.46 and 6.68 eV. The cross section Q^d , taken from [24] for energies up to 2 eV and smoothly extended to higher energies by means of that from [25], reaches very large values around 0.5 eV. The cross section for the excitation of the 6^3P_0 , 6^3P_1 and 6^3P_2 states were taken from [26] for energies up to 6 eV and were extended to higher energies by means of those from [25]. Furthermore, the cross section for the excitation of the 6^1P_1 state was taken from [27].

The geometric parameters of the cylindrical experiment arrangement were chosen to be $r_c = 0.1$ cm, $r_g = 0.8$ cm and $r_a = 1.0$ cm. These values nearly equal those of a commercially available Franck-Hertz tube [28].

In order to model the electron extraction by the grid, as mentioned above, a loss term containing the space-dependent loss frequency $\nu_g(r) = \bar{\nu}_g h(r)$ has been used. The loss has been assumed to take place just around the grid, i.e., in the region $r_g - \delta r \leq r \leq r_g + \delta r$, with the spatial averaged frequency $\bar{\nu}_g$ and the profile $h(r)$ normalised to unity according to $\int_{r_g - \delta r}^{r_g + \delta r} h(r) dr = 1$. As illustrated by the insertion in Fig. 1, the spatial electron extraction has been modelled by the shape of the sine function. Based on certain evaluations of the periodic movement of trapped electrons through the grid and the expected penetration probability of the grid, the averaged loss frequency has been fixed to $\bar{\nu}_g = 10^3 \text{ s}^{-1}$ and the width of the loss range to $2\delta r = 0.1$ cm.

Because of the very low currents in the experiment the formation of space charges can be neglected and the potential and field distribution in the cathode-grid and grid-anode region can be sufficiently described by the Poisson equation for the vacuum. This leads in each of the two regions to shapes of the form

$$V(r) = c_1 \ln r + c_2, \quad E(r) = -c_1 \frac{1}{r}. \quad (10)$$

The two pairs of resulting integration constants c_1 and c_2 can easily be determined by the conditions $V(r_g) = 0$, $V(r_c) = -U_{cg}$ and $V(r_a) = -U_{ga}$ with given positive cathode-grid and grid-anode voltages U_{cg} and U_{ga} . But this idealised choice would lead to a discontinuous field reversal at the grid position. In reality a smooth transition from the accelerating to the retarding field in the neighbourhood of the grid, with zero-crossing at the grid position has to be expected. To model such a behaviour on both sides of the grid, starting with the same distance δr from the grid as used for the loss frequency, the respective field shape according to (10) has been continuously extended to reach zero at r_g using for this range the shape of the sine function from its minimum (or maximum) to zero. The resultant profiles of the field $E(r)$ and of the associated potential energy $W(r)$ are shown in Figs. 2c and 2d for the two values 6 and 20 V of the cathode-grid voltage U_{cg} at the fixed value 1.5 V of the grid-anode voltage U_{ga} . The latter value has been used to deduce the succeeding results. The figure clearly illustrates that at lower radial positions a pronounced non-uniformity of the electric field, particularly at higher cathode-grid voltages, occurs in the experiment and that the left hand side extension of the region of trapped electrons considerably changes with the voltage U_{cg} .

In the Franck-Hertz tube the pressure p of the mercury vapour and thus the gas density N is determined by the vapour temperature T . This dependence is approximately described with p in mTorr and T in K units by the relation [29]

$$\ln p(T) = 30.804 - 0.8254 \ln T - 7564 / T. \quad (11)$$

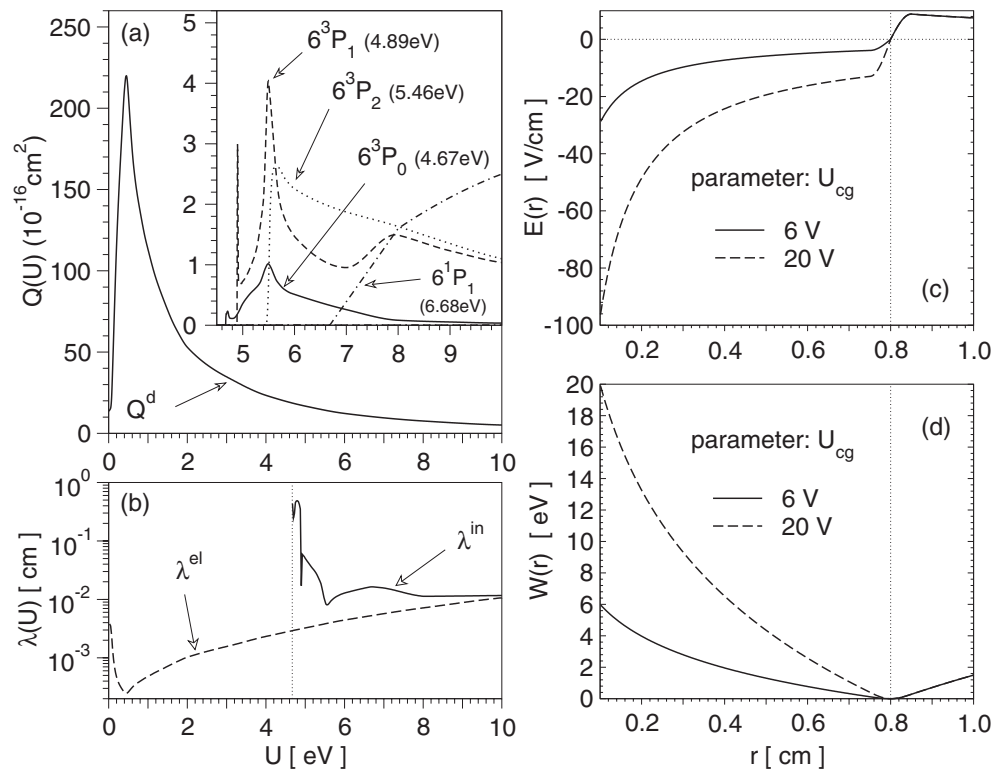


Fig. 2 Input data for the kinetic treatment: (a) Cross section of the electron-atom collisions in mercury, (b) mean free path of the electrons due to elastic (λ^{el}) and inelastic (λ^{in}) collisions, (c) electric field $E(r)$ and (d) potential energy $W(r)$ for $U_{cg}=6$ and 20 V.

A temperature of 180° C has been supposed for the analysis, i.e., the study has been performed at a gas density N of $18.4 \times 10^{16} \text{ cm}^{-3}$ related to a pressure p of 8.6 Torr. Using this gas density and the collision cross sections given in Fig. 2a the mean free path $\lambda^{el}(U) = 1/(N Q^d(U))$ and $\lambda^{in}(U) = 1/(\sum_l N Q_l^{in}(U))$ of the elastic and inelastic collisions in mercury have been determined and represented in Fig. 2b. Especially the shape of λ^{el} clearly shows the extremely small mean free path of low energy electrons in elastic collisions compared with the cathode-grid distance. Thus, the above assumption concerning the immediate formation of a widely isotropic velocity distribution of the electrons, released by the thermionic emission, should be quite justified.

The energy distribution of the thermionic electron emission according to (6) has been fixed by an emitter temperature of $T = 1500^\circ \text{ K}$ [18] and an electron density at the cathode of $n(r_c) = 10^5 \text{ cm}^{-3}$. Because of the complete linearity of the kinetic problem (3) to (9), the choice of the electron density $n(r_c)$ ultimately serves for the normalization of both distributions \bar{f}_0 and \bar{f}_r and, consequently, of the resultant macroscopic quantities.

Furthermore, an electron reflection at the anode of 80 % has been assumed [30], i.e., $\rho = 0.8$ is used in the boundary condition (7).

5 Results and discussion

After the solution of the kinetic problem (3) to (9) for specified parameter conditions of the experiment, the corresponding spatial profiles of all relevant macroscopic properties of the electrons can be deduced by appropriate energy space averaging over the isotropic and anisotropic distribution $\bar{f}_0(U, r)$ and $\bar{f}_r(U, r)$, respectively. When performing the solution approach for a larger sequence of cathode-grid voltages U_{cg} at fixed grid-anode voltage U_{ga} finally the well-known anode current characteristics of the Franck-Hertz experiment can be obtained.

5.1 Electron flux characteristics and transport properties

From the representation (2) of the velocity distribution function the expressions

$$n(r) = \int_0^\infty U^{1/2} \bar{f}_0(U, r) dU, \quad (12)$$

$$u_m(r) = \int_0^\infty U^{3/2} \bar{f}_0(U, r) dU / n(r), \quad (13)$$

$$j_r(r) = \frac{1}{3} \sqrt{2/m_e} \int_0^\infty U \bar{f}_r(U, r) dU, \quad (14)$$

$$j_{er}(r) = \frac{1}{3} \sqrt{2/m_e} \int_0^\infty U^2 \bar{f}_r(U, r) dU \quad (15)$$

for the electron density $n(r)$, the mean energy $u_m(r)$ and the particle and energy flux density $\vec{j}(r) = j_r(r) \vec{e}_r$ and $\vec{j}_e(r) = j_{er}(r) \vec{e}_r$ can be derived.

Because of the cylindrical geometry the radial particle and energy flux of the electrons through the cylindrical shell per unit of the cylinder's length at the position r is given by $J_r(r) = 2\pi r j_r(r)$ and $J_{er}(r) = 2\pi r j_{er}(r)$.

Furthermore, the electron particle balance, consistent with the considered kinetic problem (3) to (9), reads

$$\frac{1}{r} \frac{d}{dr} (r j_r(r)) = -\nu_g(r) n(r) \quad (16)$$

and its formal solution is given by

$$J_r(r) = J_r(r_c) - 2\pi \int_{r_c}^r \nu_g(\hat{r}) n(\hat{r}) \hat{r} d\hat{r}. \quad (17)$$

Thus, owing to the spatially limited electron extraction, the flux $J_r(r)$ remains constant in the region $r_c \leq r \leq r_g - \delta r$ and equals the cathode flux $J_r^c \equiv J_r(r_c)$. Similarly, $J_r(r)$ does not change in the region $r_g + \delta r \leq r \leq r_a$ and represents there the anode flux $J_r^a \equiv J_r(r_a)$.

Instead of the electron currents the electron particle fluxes per unity of the cylinder length J_r , J_r^c and J_r^a will be used in the succeeding presentation of the results of the kinetic study.

For the parameters given above, the cathode and anode flux, obtained by the solution of the kinetic problem for a sequence of about 80 cathode-grid voltages U_{cg} , is displayed in Fig. 3a showing the dependence on U_{cg} . Apart from the pronounced increase of the cathode flux the experimentally well known oscillating structure and an increasing amplitude of the oscillation of the anode flux can be clearly observed with growing U_{cg} from this figure. The acceleration voltages related to the anode flux maxima and minima are marked in this figure, and in Figs. 3b,c as well, by vertical dotted and dashed lines, respectively. Furthermore, the numbers presented additionally in the figure approximately give (starting from left hand side) the voltage of the first anode flux maximum and the voltage differences between successive maxima of the anode flux. The first voltage and the further voltage differences are the crucial values in the framework of the interpretation of the Franck-Hertz experiment. According to various textbook explanations of the experiment mentioned above they should be all equal to the threshold energy of the mercury excitation. But obviously this is not strictly the case and considerable deviations, particularly with respect to the first maximum, from this expectation are found by the kinetic study of this famous experiment. This point will be considered more in detail below in the framework of the analysis of the energy transfer processes, to make the reasons for these deviations on the basis of the complex behaviour of the electron gas under real experimental conditions more understandable.

In order to present a detailed overview of the variation of the transport properties with the applied cathode-grid voltage U_{cg} , the spatially resolved behaviour of the density n , mean energy u_m and of the particle and energy flux J_r and J_{er} are shown in Fig. 4 for the first three maxima and the second minimum of the anode flux J_r^a , i.e., for $U_{cg} = 5.0, 9.62, 11.5$ and 14.35 V.

In all four cases a large spatial variation of the electron density, always starting from the value 10^5 cm^{-3} in front of the cathode, can be observed. After some oscillations, that occur at not too small voltages U_{cg} , a large

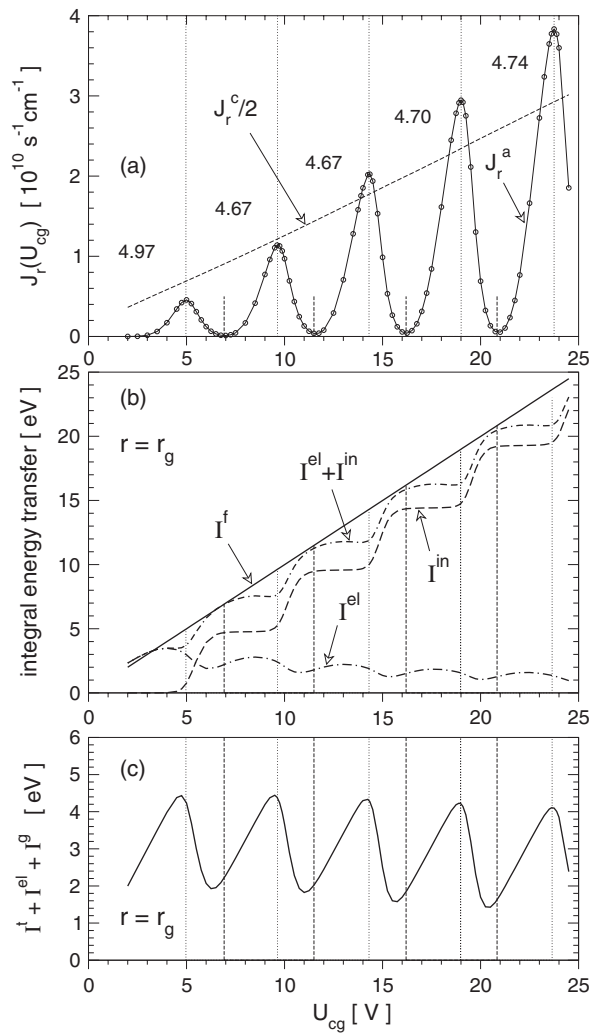


Fig. 3 Variation of macroscopic quantities of the electrons with the accelerating voltage U_{cg} at a mercury vapor temperature of 180°C (correspondingly $p = 8.6 \text{ Torr}$, $N = 18.4 \cdot 10^{16} \text{ cm}^{-3}$). (a) Cathode and anode flux, (b) spatially integrated energy gain and losses and (c) lumped loss $I^t + I^{el} + I^g$.

increase of the density by almost two orders of magnitude around the grid position, i.e., around the minimum of the valley of the potential energy W , occurs. Then, towards the anode a strong density decrease far below the original value close to the cathode takes place because of the decreasing influence of electron capture and the overlapping influence of the electron absorption at the anode. The density oscillations in the cathodic region are very similar to former results on the spatial electron relaxation [11–13] initiated by local disturbances of the velocity distribution function or by non-uniformities of the electric field. In the cathodic region the density related to the second minimum of the anode flux behaves very similar to that at the maxima, but becomes the largest at the minimum position of W and the smallest at the anode because of the large electron capture that especially occurs if the anode flux approaches its minimum.

The representation in Fig. 4 shows that the mean energy u_m of the electrons amounts to about 0.3 eV close to the cathode, passes through considerable oscillations with an amplitude of few eV in the cathodic region, assumes very small values of about 0.05 eV around the region of the strongest electron capture and approaches values of about 1 eV close to the anode. The mean energy belonging to the minimum of the anode flux remains markedly smaller in the broader surrounding of the grid compared to the cases associated with the neighbouring maxima of the anode flux. This is a reflection of the large electron capture close to the grid in this case.

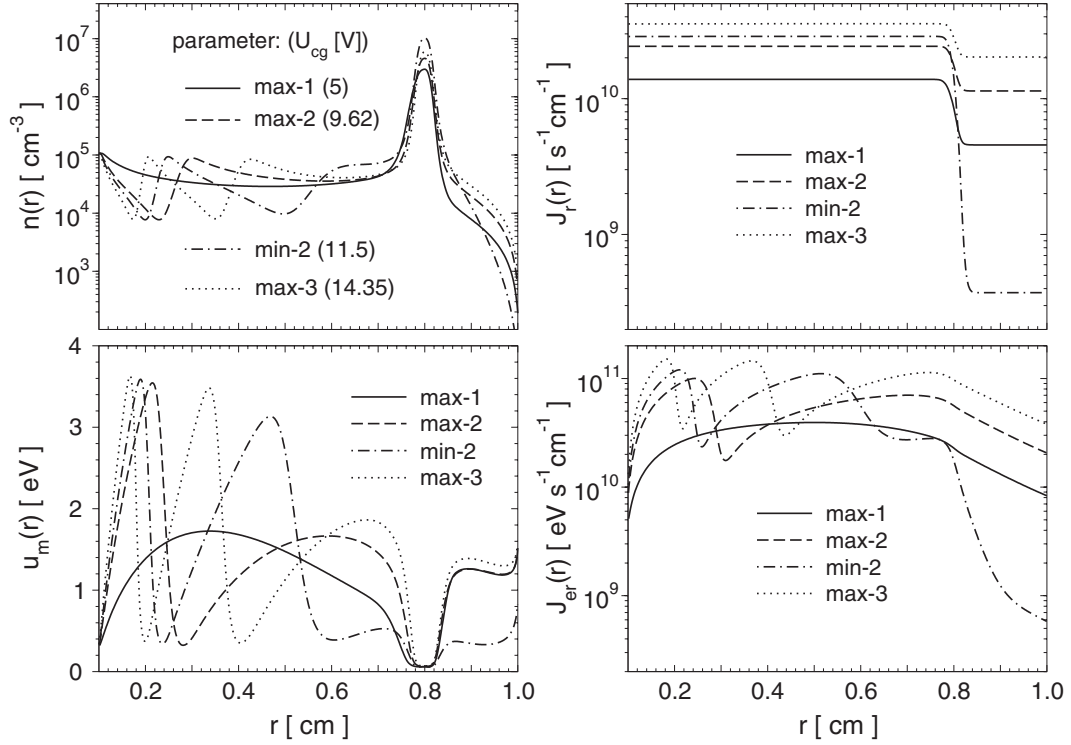


Fig. 4 Spatial variation of macroscopic quantities for selected values of the accelerating voltage U_{cg} at a mercury vapor temperature of $T = 180^\circ\text{C}$.

The representation of the electron flux J_r for the same anode flux conditions shows that in all four cases a pronounced change of the flux J_r takes place in the immediate vicinity of the grid position. This almost abrupt change is mainly caused by the overlapping peak-like profiles of the extraction frequency $\nu_g(r)$ and the density $n(r)$ of the trapped electrons close to r_g . The fact that the flux J_r varies only in the region close to the grid is in complete agreement with the above conclusions deduced from the particle balance (16) and its formal solution (17).

The right bottom part of Fig. 4 presents the spatial behaviour of the energy flux J_{er} per unit length of the cylinder. In all four cases a rapid increase of the energy flux starting from its low value at the cathode can be observed. In the cathodic part the oscillating behaviour of J_{er} is similar to that of the density n . Despite the considerable increase of the electron density around the grid and the almost abrupt decrease of the electron flux in this region a more smooth change around the grid is obtained followed by a larger decrease of the energy flux when approaching the anode. Under the condition of anode flux minimum, i.e., large electron capture close to the grid, the energy flux towards the anode becomes also very small.

To give a certain overview on some transport properties in the grid-anode region with respect to the same broad range of the cathode-grid voltages, as considered in Fig. 3a, the Figs. 5a,b show the density n and the mean energy u_m of the electrons as a function of U_{cg} at the grid position r_g and halfway between the grid and the anode, i.e., at $r_{ga} \equiv (r_g + r_a)/2$. The acceleration voltages related to the anode flux maxima and minima are marked in these figures by the same vertical lines as in Figs. 3a-c. Orders of magnitude different densities at the grid and halfway from the grid to the anode, but further on in the potential energy valley, can be observed from Fig. 5a at all acceleration voltages. In a certain sense an opposite behaviour results for the mean energy at r_g and r_{ga} with significantly higher mean energies at r_{ga} compared to those in the minimum of the potential energy valley. Furthermore, some fixed phase relations obviously occur in these figures, especially between the minima of the density at r_g and the anode flux maxima and between the minima of the mean energy at r_{ga} and the anode flux minima.

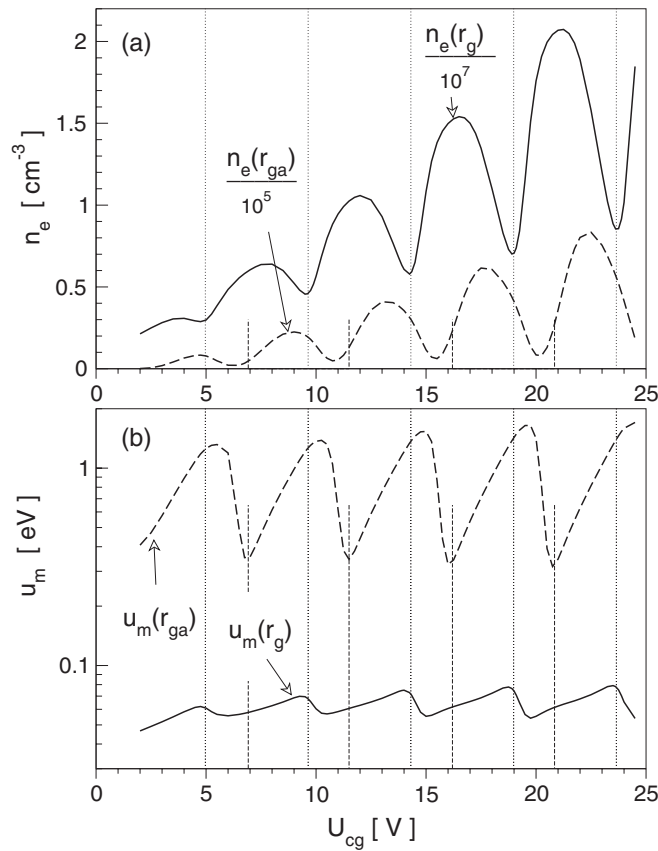


Fig. 5 Variation of (a) the density and (b) mean energy of the electrons at the positions r_g and r_{ga} with the accelerating voltage U_{cg} at a mercury vapor temperature of 180°C .

5.2 Energy space resolved electron behaviour

For the three cathode-grid voltages 9.62, 11.5 and 14.35 V, associated with the second maximum, the second minimum and the third maximum of the anode flux in Fig. 3a, the contour plots of the isotropic part $f_0(\varepsilon, r)$ and, in reduced form in the insertion, those of the anisotropic part $f_r(\varepsilon, r)$ are shown in Fig. 6 over the corresponding (ε, r) -area. The lower ε -border of both distribution parts corresponds to the limit of vanishing kinetic energy U and presents, according to $\varepsilon = U + W(r)$, the shape of the potential energy $W(r)$. In each plot, the horizontal dot-dash line at $\varepsilon = U_{ga}$ marks the region of trapped electrons that extends below this line from the left short vertical line up to the anode.

Owing to the thermionic emission the electrons start at r_c with a narrow, isotropic distribution of low kinetic energies and are accelerated towards the grid by the action of the large cathodic field, as it is obvious from Fig. 2c. On their way they undergo elastic and inelastic collisions exciting the atoms. As a result of the small amount of the energy loss in each elastic collision the contours of the isotropic distribution smoothly decline towards smaller total energies. But, due to each exciting collision, the respective electron loses the corresponding threshold energy U_i^{in} and jumps down by this energy to a lower total energy, at an unchanged spatial position. By this latter process a further group of electrons occurs at lower ε and the overall process, just illustrated, of field action and collisions can continue a few times, largely depending on the overall magnitude $W(r_c) = e_0 U_{cg}$ of the potential energy considered. However, when approaching the left margin of the potential energy valley with increasing r , i.e., the region of trapped electrons, the situation completely changes. Electrons, depending upon their energy as they approach the left margin of the potential energy valley, can either remain energetically above the valley up to the anode, or become trapped in the valley before reaching the anode. If the first case applies to the majority of the electrons a large anode flux occurs and such situations are illustrated by the upper and lower

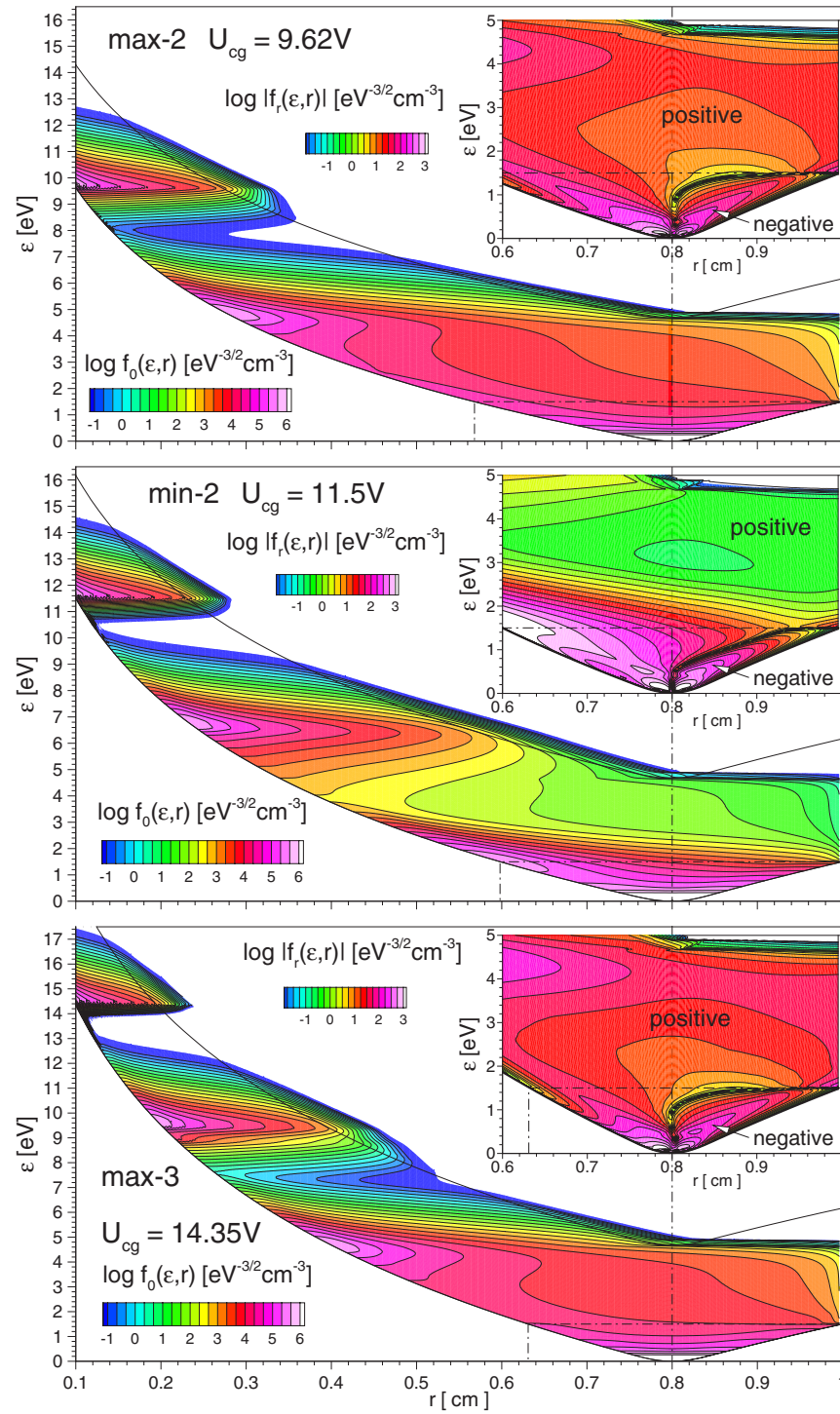


Fig. 6 Contour plot of the isotropic and anisotropic part of the electron velocity distribution function for the accelerating voltages $U_{cg} = 9.62, 11.50$ and 14.35 V.

part of Fig. 6. In the opposite extreme, as displayed by the centre part of this figure, the larger part of the electrons are trapped on their way towards the anode and a low anode flux only occurs. Which of the different energetic

conditions, that are possible close to the left margin of the potential energy valley, ultimately emerge, depends on several parameters of the experiment and at fixed geometry and mercury vapour pressure, in particular, on the magnitude of the cathode-grid voltage U_{cg} .

Because of the moderate change and smaller magnitude of the electric field in the region close to the left margin of, and within the potential energy valley a larger energy loss in elastic collisions and, consequently, a stronger decline of the contours of f_0 becomes obvious in all three f_0 representations of Fig. 6. This largely contributes to the very efficient electron capture by the potential energy valley. Therefore, even those electrons which suffer inelastic collisions already somewhat before reaching the left margin of the potential energy valley are finally captured.

According to the relation (14) the flux density j_r close to the anode, and thus the flux per unit length J_r , are primarily determined by the energy space average over the anisotropic distribution in this spatial region. The magnitude of the transformed anisotropic part $f_r(\varepsilon, r) \equiv \bar{f}_r(\varepsilon - W(r), r)$ is shown in this region by the insertions in Fig. 6. Rather low values of the positive part of f_r can be observed close to the anode in the centre part (min-2) of the figure however considerably larger values of the positive part of f_r in the upper (max-2) and lower part (max-3) of Fig. 6. Furthermore, the representations of the anisotropic distributions clearly show that generally in the grid-anode region a negative part appears in these distributions at low kinetic energies. This negative part describes the back flow of the trapped electrons towards the grid in the retarding branch of the potential energy.

To illustrate the energy dependence of both distribution parts more in detail, Fig. 7 displays, for the same cathode-anode voltages as considered in Fig. 4, the distributions $\bar{f}_0(U, r)$ and $\bar{f}_r(U, r)$ as a function of the kinetic energy U at the grid position (left) and halfway between the grid and the anode (right), i.e., at r_g and r_{ga} . The upper energy margin of the potential energy valley at these positions is additionally marked by vertical dotted lines in all parts of the figure. For comparison, the isotropic distribution $\bar{f}_0(U, r_c)$ in front of the cathode, fixed by the boundary condition (5), is additionally shown in the left upper part of the figure.

At the grid position a maximum in the population of low energy electrons in the isotropic distribution can be seen as a consequence of the strong electron capture around the minimum of the potential energy valley. In the energy range of a few eV, a considerable variation of the population of \bar{f}_0 , and of \bar{f}_r as well, arises with consecutive orders of the maxima of the anode flux and, in particular, with the transition from the maximum to the neighbouring minimum. In particular, the modulation of \bar{f}_r coincides with the corresponding one of the anode flux. The anisotropic distributions at grid position are generally small, because of the field reversal at this position, and possess a somewhat unexpected structure. Thus, in the distributions belonging to the first and third anode flux maxima, an intermediate negative part just below 1 eV even occurs, possibly due to some overshooting in the back flow of the captured electrons from the adjacent retarding potential region.

Both parts of the distribution at the halfway position of the retarding potential energy branch, i.e., at r_{ga} , no longer possess the low energy part of the captured electrons present in the distribution parts at r_g , and seems, from rough considerations, to be associated with a shift to smaller kinetic energies of the corresponding distributions at r_g . However, in all anisotropic distributions a considerable negative part at lower energies appears, which reflects the backward electron flux caused by the reverse electric field in the grid-anode range. The upper energy margin of the negative part of the anisotropic distributions at r_{ga} is almost the same for the three anode flux maxima, and extends up to about the upper margin of the potential energy valley at this position.

For a somewhat broader spatial range this can clearly be seen from the representation of $f_r(\varepsilon, r)$ in the insertions of Fig. 6. However, the extent of the negative part of the anisotropic distribution shows a considerable variation with the applied cathode-grid voltage U_{cg} . This fact becomes quite obvious when comparing in Fig. 6 the corresponding distributions related to a maximum and the minimum of the anode flux.

5.3 Evaluation of the power gain and loss processes

In order to characterise the behaviour of the electron gas from the energetic point of view, the energy transfer processes occurring in the experiment have to be analysed on a kinetic basis.

The consistent power balance equation of the electron gas can be derived by appropriate energy space averaging over the lowest hierarchy equation (3) and can be given the representation

$$P^t(r) = P^f(r) - P^{el}(r) - P^{in}(r) - P^g(r), \quad (18)$$

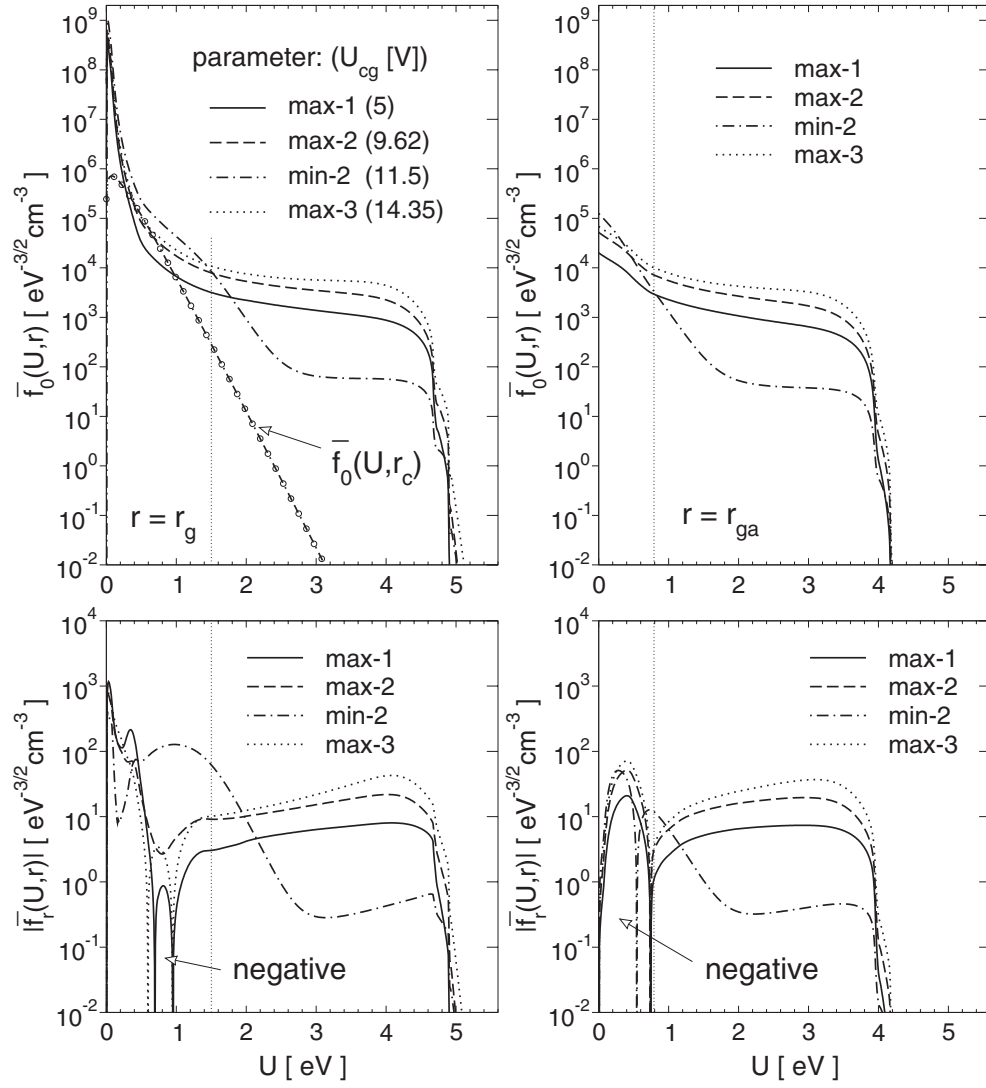


Fig. 7 Velocity distribution components for selected values of the accelerating voltage U_{cg} at a vapor temperature of 180°C . The vertical dotted lines mark the energy boundary between trapped and free electrons.

where

$$P^t(r) = \frac{1}{r} \frac{d}{dr} (r j_{er}(r)), \quad (19)$$

$$P^f(r) = -j_r(r) e_0 E(r), \quad (20)$$

$$P^{el}(r) = 2 \frac{m_e}{M} \sqrt{2/m_e} \int_0^\infty U^2 N Q^d(U) \bar{f}_0(U, r) dU, \quad (21)$$

$$P^{in}(r) = \sum_l U_l^{in} \sqrt{2/m_e} \int_0^\infty U N Q_l^{in}(U) \bar{f}_0(U, r) dU, \quad (22)$$

$$P^g(r) = \nu_g(r) u_m(r) n(r). \quad (23)$$

The expression (19) describes, via the divergence of the energy flux density j_{er} , the power loss or gain P^t at the position r caused by the transport of kinetic energy. Furthermore, the power gain P^f from the electric field, the

power loss in elastic (P^{el}) and inelastic (P^{in}) collisions and the power loss P^g due to the electron extraction by the grid are given by the expressions (20) to (23).

For the same four maximum and minimum conditions of the anode flux as considered in Fig. 4, the spatial variation of the power losses P^{el} and P^{in} in elastic and inelastic collisions and, for comparison, the power gain P^f from the field are displayed in Fig. 8. Because of the field reversal in the grid-anode range, the field term P^f becomes negative between $r = 0.8$ and 1.0 cm, and represents here always a power loss of the electrons in the retarding field. In addition, the left margin and the minimum position of the potential energy valley are marked in each part of the figure by thin vertical lines.

The upper part of the figure, related to the condition of the first anode flux maximum, shows that the loss in elastic collisions P^{el} dominates in this case to a large extent over the loss in inelastic collisions P^{in} , and this dominance holds in the entire range between the cathode and the anode. Thus, this fact is in obvious contradiction to some textbook interpretations of the first anode flux maximum according to which the energy loss in elastic collisions is completely neglected compared with the inelastic loss.

Furthermore, the shape of the inelastic losses in this figure makes it obvious that the first inelastic collisions already appear significantly before the grid position, i.e., when the electrons have suffered an accelerating voltage still markedly smaller than the lowest excitation energy of 4.67 eV. The latter effect doubtless results from the energy of the electrons available in the tail of the isotropic distribution $f_0(U, r_c)$ at the cathode boundary, shown in the left upper part of Fig. 7.

With increasing cathode-grid voltage U_{cg} , i.e., in the further three parts of Fig. 8, the overall role played by P^{el} continuously decreases, but remains significant, particularly in the field reversal range, where primarily trapped electrons of low energy are present.

The parts of the figure related to the three anode flux maxima clearly exhibit, with growing number of maxima, the same increasing number of spatial ranges where inelastic collisions occur. The width of these inelastic collision regions grows when going at fixed U_{cg} from the cathode to the grid and the width, e.g., of the first cathode-sided inelastic collision region, decreases with growing voltage U_{cg} . These peculiarities primarily result from the distinct increase of the radial variation of the potential profile $W(r)$ or the field profile $E(r)$ especially in the cathodic region at fixed U_{cg} and the drastic amplification of this property with growing voltage U_{cg} , as shown in Figs. 2c and 2d.

In the three cases of maximum anode flux the considerable spatial extent of the grid-sided region of the inelastic losses with a left margin significantly away from the grid position makes quite clear that the conventional textbook explanations of the formation of an anode flux maximum is in some contradiction to the reality and presents a substantial idealisation.

When comparing the two centre parts of Fig. 8 related to the second anode flux maximum and minimum rather different magnitudes of the grid-sided contributions to P^{in} can be observed. In the case of minimum anode flux ($U_{cg} = 11.5$ V) significantly larger energy losses in inelastic collisions, occurring in a broader range markedly before the grid position, can be observed and consequently a distinctly stronger electron capture around the grid takes place at minimum anode flux or maximum extraction by the grid.

In order to get a more detailed evaluation of the energy transfer processes which proceed between the cathode and the anode and, especially, up to the grid position, a spatially integrated version of the power balance equation (18), normalized before on the macroscopic electron flux $J_r(r)$, yields the appropriate basis. Thus, with the integral operation

$$I^i(r) = 2\pi \int_{r_c}^r \frac{P^i(\hat{r})}{J_r(\hat{r})} \hat{r} d\hat{r}, \quad i = t, f, el, in, g \quad (24)$$

from (18) the spatially integrated power balance

$$I^t(r) = I^f(r) - (I^{el}(r) + I^{in}(r) + I^g(r)) \quad (25)$$

is obtained. In particular, the application of (24) to the field term $P^f(r)$ of (18) yields the expression

$$I^f(r) = -e_0 \int_{r_c}^r E(\hat{r}) d\hat{r} = W(r_c) - W(r) = e_0 U_{cg} - W(r). \quad (26)$$

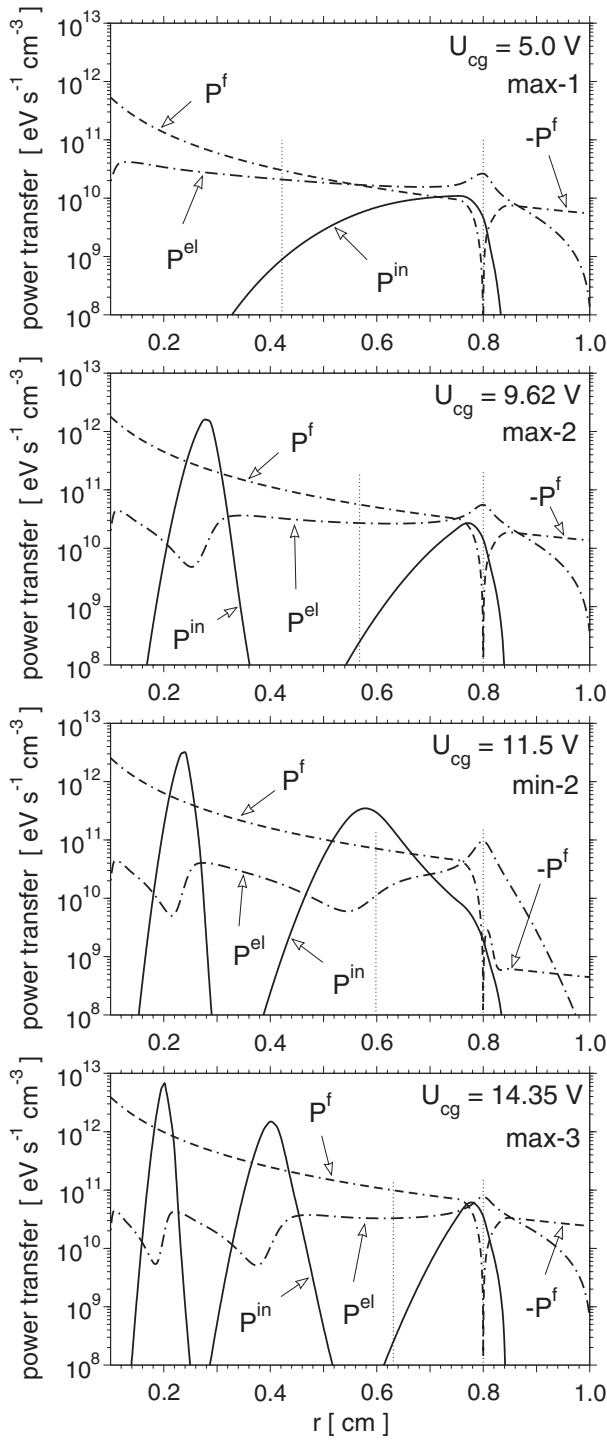


Fig. 8 Power transfer for selected values of the accelerating voltage U_{cg} at $T = 180^\circ\text{C}$.

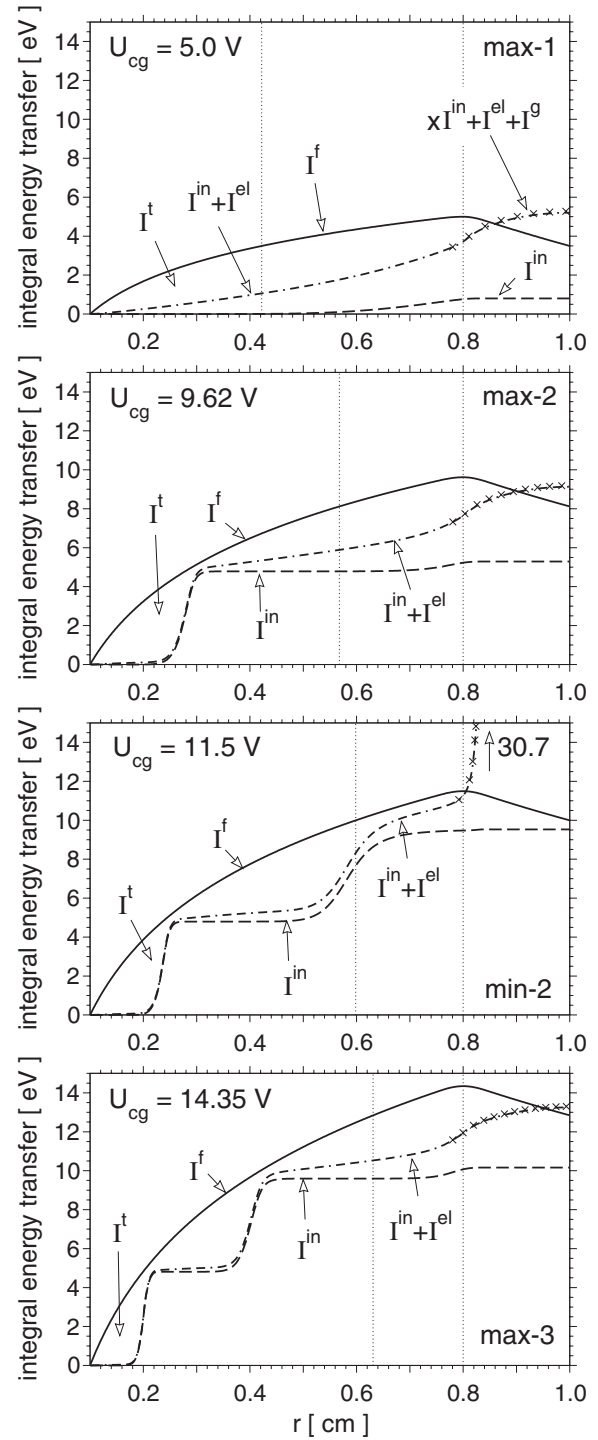


Fig. 9 Integrated energy transfer for selected values of the accelerating voltage U_{cg} at $T = 180^\circ\text{C}$.

Thus, the power input per flowing electron I^f accumulated between the cathode and the position r simply equals the gain per electron from the potential energy between these positions. Correspondingly, the other terms $I^i(r)$, $i = el, in, g, t$ in the integrated power balance (25) represent the losses in elastic and inelastic collisions,

the loss by the grid extraction and the loss or gain by the energy transport which took place per flowing electron on its way from the cathode to the position r .

The representation of these accumulated gains and losses is given in Fig. 9 for the same four anode flux conditions as considered in Figs. 4, 7 and 8. More in detail, the figures show the spatial behaviour of I^f , I^{in} , $I^{in} + I^{el}$ and $I^{in} + I^{el} + I^g$; the latter above $r_g - \delta r$, where I^g becomes non zero. The comparison between the dot-dash-dash line and the crosses above r_g indicates that the loss I^g , caused by the grid extraction of the trapped electrons with very low kinetic energy, is always very small and can be neglected in the further discussion. The difference area between I^f and $I^{in} + I^{el} + I^g$ gives the contribution of the transport term I^t to the integrated power balance (25).

The upper part of the Fig. 9 related to the first anode flux maximum clearly shows that a considerable part of the invested field energy I^f is increasingly transferred with growing r to the mercury atoms by the loss in elastic collisions I^{el} . The accumulated inelastic loss I^{in} is always small and this happens as well around the grid position. The consideration of the three figures related to the anode flux maxima clearly illustrates that the accumulated elastic loss I^{el} decreases, especially in the cathodic region, with growing number of the maxima in comparison with the accumulated inelastic loss I^{in} . However, in the range around the grid a portion of some eV of the invested field energy I^f is always covered by elastic collisions. The reduced role played by the elastic loss in the cathodic region with growing voltage U_{cg} results from the significant increase of the electric field in this region as being illustrated in Fig. 2c. All parts of Fig. 9 well demonstrate with growing r by the step-like increases of the accumulated inelastic loss I^{in} the spatially limited regions where significant contributions to I^{in} arise. Especially the figures related to the anode flux maxima show that under this condition always the next increase of I^{in} starts just before the grid position and proceeds here still in a rather smooth manner. This slight increase is the realistic reflection of the idealized textbook explanation that when reaching the anode flux maximum with growing U_{cg} the electrons just become capable to undergo inelastic collisions at the grid position.

A comparison of the figure parts belonging to the second maximum and second minimum clearly demonstrates that a much better characterization of the accumulated inelastic losses I^{in} at the grid position becomes possible at minimum anode flux because of its nearly space-independent value around the grid. The vertical distances between the horizontal parts of the accumulated inelastic loss I^{in} can be interpreted to present the effective energy loss per flowing electron and per inelastic collision event of the mainly involved excitation processes, i.e., of the lowest two inelastic loss channels in mercury. Under the minimum condition almost all electrons that reach r_g have suffered inelastic collisions in a certain region before the grid and are trapped in the minimum range of the potential energy valley, but largely in consequence of the further energy losses in elastic collisions.

In all parts of Fig. 9 the term I^t related to the accumulated energy transport per flowing electron varies around a considerable magnitude, is positive in the cathode-grid region and becomes negative in the grid-anode region. This means that in almost the entire spatial range a considerable portion of the invested field energy I^f is lastly contained in the power source and sink contribution arising from the pronounced non-uniformity of the energy flux J_{er} and this part does not be available to contribute to the power loss in collisions. This term is an immediate consequence of the distinct nonlocal character of the power transfer under the parameter conditions of the experiment. At maximum anode flux always a portion of several eV of the invested field energy I^f is covered by the transport term I^t in the region close to the grid. However, at minimum anode flux the accumulated transport term I^t passes through zero very close to the grid position. Then, apart from the invested field energy, the important contributions to the integrated power balance per flowing electron (25) are only those by the inelastic and elastic collisions at the grid position.

To provide a more complete overview in a broader range of the cathode-grid voltage, the energy transfer contributions per flowing electron, accumulated between the cathode and the grid position, are shown in Fig. 3b as a function of U_{cg} . Apart from the field term I^f again the losses I^{in} , $I^{el} + I^{in}$ and additionally I^{el} are displayed at $r = r_g$. The difference between I^f and $I^{el} + I^{in}$ represents according to (25) the accumulated transport term I^t . Furthermore, as in Fig. 3a, the accelerating voltages related to the anode flux maxima are marked by vertical dotted lines and the minima by vertical dashed lines. The behaviour of I^{in} with growing U_{cg} clearly shows that at about the respective U_{cg} voltage of all five anode flux maxima the electron gas becomes increasingly capable to undergo inelastic collisions and that at about the respective U_{cg} voltage of the four anode flux minima the electrons become increasingly incapable to perform inelastic collisions close to the grid position.

Furthermore, the Fig. 3b shows that at all maximum voltages an amount of a few eV of the invested field energy I^f is transferred by the elastic loss I^{el} as well as by the transport term I^t . Whilst the portion of the elastic loss slowly decreases with increasing flux maximum voltage an opposite nature results for the portion of the transport term I^t . Almost the same variation of the elastic loss proportion can be observed with growing flux minima voltages, however, the proportion of the transport term is almost negligible at all flux minima voltages. As mentioned above, according to the simplified explanation of the anode flux maxima formation the invested field energy I^f should be largely transferred by the accumulated loss in inelastic collisions I^{in} . However, the integrated balance (25) only says $I^f(r_g) - I^{in}(r_g) = I^t(r_g) + I^{el}(r_g) + I^g(r_g)$, i.e., the difference between the field term and the inelastic loss is given by the lumped term $I^t + I^{el} + I^g$ mainly containing the elastic loss and the loss due to the nonuniform energy transport. This lumped term is additionally displayed in Fig. 3c in dependence on U_{cg} . Its contribution to the integrated balance at $r = r_g$ amounts to several eV in the entire U_{cg} range and, unexpectedly, assumes an almost constant value of about 4 eV at all anode flux maxima.

5.4 Anode flux characteristics and energy transfer at different mercury pressures

As a result of the complex interplay of the invested field energy I^f and the dominant energy loss and transport processes I^{in} , I^{el} and I^t in the electron gas the anode flux characteristics shown in Fig. 3a is formed. This interplay has been illustrated in a radially resolved form for some anode flux maxima and one minimum in Fig. 8 and in dependence on the accelerating voltage U_{cg} for the grid position r_g in Figs. 3b,c. From these figures it can be clearly seen that the first anode flux maximum is entirely dominated by elastic losses. Consequently its corresponding acceleration voltage of 4.97 V does not present a reflection of the lowest energy threshold of the mercury excitation. Its value is about 0.3 eV larger than the lowest excitation threshold of 4.67 eV and this happens despite the additionally available mean energy $u_m(r_c)$ of about 0.3 eV of the emitted electrons at the cathode. At this low acceleration voltage related to the first flux maximum the lowest mercury excitation process is the only one of importance.

However, the voltage differences between the successive anode flux maxima, additionally given in Fig. 3a, are obviously a good reflection of the energy loss in inelastic collisions per flowing electron under the considered parameter conditions. This conclusion is mainly based on the almost constant value of the lumped loss $I^t + I^{el} + I^g$ at all anode flux maxima shown in Fig. 3c. Consequently, when taking the difference between two applications of the accumulated balance (25) for $r = r_g$ to successive anode flux maxima the corresponding difference between the two lumped losses $I^t + I^{el} + I^g$ largely compensate each other. Then, the corresponding difference of the invested field energies I^f largely equals the difference of the inelastic losses I^{in} . Furthermore, the slight increase of the corresponding difference energies from 4.67 eV to 4.74 eV in Fig. 3a indicates the weak shift from dominant energy loss by the lowest excitation process to a certain contribution of the second excitation processes with the threshold energy of 4.89 eV when increasing the accelerating voltage to about 24 V.

The anode flux characteristics in Fig. 3a has been derived for a mercury vapour pressure of 8.6 Torr related to a temperature of 180° C. As to be seen from this figure, the saturation of the anode flux with respect to the cathode flux amounts to about 50 % under these conditions. To illustrate especially the influence of the vapour pressure on the structure of the characteristics, the resultant anode flux saturation and on the energy transfer processes accumulated between the cathode and the grid, the Figs. 10 and 11 display these quantities at the pressures of 16.9 and 2.8 Torr which belong to vapour temperatures of 200° C and 150° C and to gas densities of $34.4 \times 10^{16} \text{ cm}^{-3}$ and $6.39 \times 10^{16} \text{ cm}^{-3}$, respectively. All other parameters, especially those of the electric field and the cathode- and anode-sided boundary conditions, have been kept unchanged. The corresponding maxima and minima voltages of the anode flux are again indicated by vertical dotted lines and dashed lines as done in Figs. 3a-c.

In the first case a very low saturation of about 10% and in the second case an almost 100% saturation of the anode flux is obtained for accelerating voltages around the anode flux maxima. Correspondingly, the Fig. 10b shows a markedly enhanced contribution and Fig. 11b a very small contribution of the accumulated elastic loss per flowing electron I^{el} compared with the contribution I^{el} in Fig. 3b. However, quite the reversal behaviour can be observed with respect to the contribution of the transport term I^t , given by the difference between I^f and $I^{el} + I^{in}$. With increasing pressure a distinct transition toward a local energy transfer, i.e., with negligible contributions of the transport term I^t to the spatially integrated power balance is found.

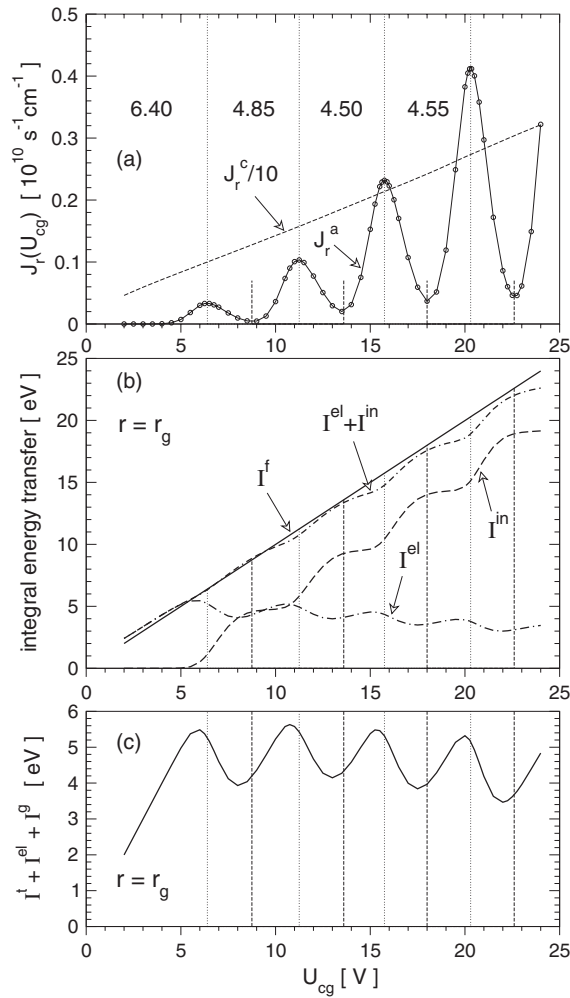


Fig. 10 Variation of macroscopic quantities of the electrons with the accelerating voltage U_{cg} at a vapor temperature of 200°C (correspondingly $p = 16.9 \text{ Torr}$, $N = 34.4 \cdot 10^{16} \text{ cm}^{-3}$). (a) Cathode and anode flux, (b) spatially integrated energy gain and losses and (c) lumped loss $I^t + I^{el} + I^g$.

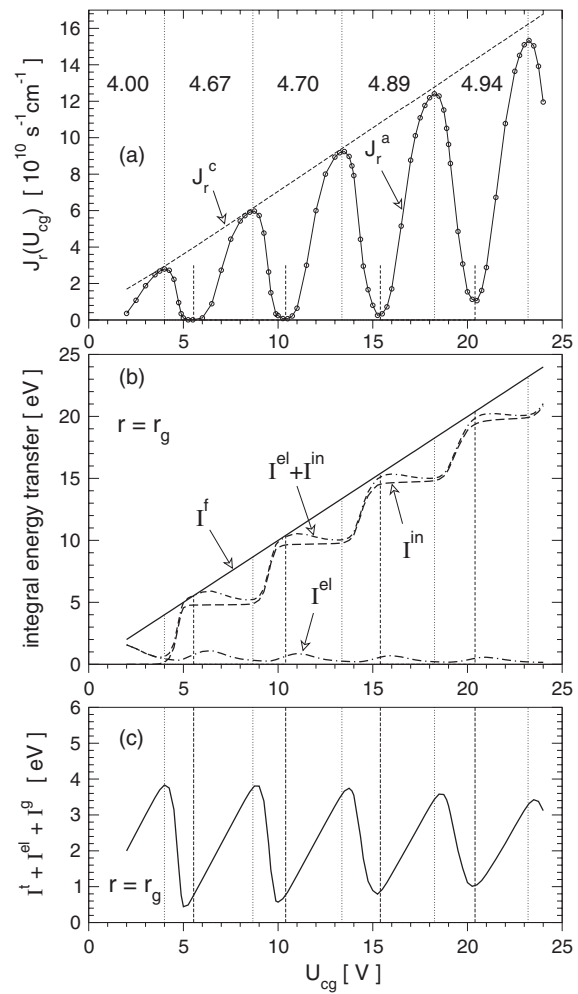


Fig. 11 Variation of macroscopic quantities of the electrons with the accelerating voltage U_{cg} at a vapor temperature of 150°C (correspondingly $p = 2.8 \text{ Torr}$, $N = 6.39 \cdot 10^{16} \text{ cm}^{-3}$).

An immediate consequence of the varied pressure and the resultant change of I^{el} is the significant variation of the accelerating voltage related to the first anode flux maximum. The corresponding energies are 6.40 eV at the higher pressure and 4.00 eV at the lower pressure as indicated by the first number on the left hand side in the figures. Furthermore, the Figs. 10b and 11b clearly demonstrate that the spectrum of difference energies related to the successive anode flux maxima slightly decrease, even below the lowest threshold energy, at the higher pressure, however slightly increase at the lower pressure. In the first case the stronger elastic losses mainly determine this variation whilst in the latter case the pronouncedly nonlocal energy transfer as exhibited by the transport term I^t and the shift in the dominance of the two lowest inelastic loss channel exert the main influence on the difference energy variation. But in both these cases the derived difference energies remain close to the threshold energies of the two lowest mercury excitation processes which are the only dominant inelastic loss channels under the considered parameter conditions. This latter conclusion is again based on the behaviour of the lumped loss $I^t + I^{el} + I^g$ at $r = r_g$ shown in Figs. 10c and 11c for the higher and lower vapour pressure. According to these results the lumped loss assumes almost the same value at all acceleration voltages related to anode flux maxima.

6 Conclusions

In recent years a considerable progress concerning the detailed study of the spatially one-dimensional kinetics of the electrons, moving in a neutral gas under the action of a pronouncedly non-uniform electric field and even a field reversal and undergoing various types of binary collisions with the gas particles, has become possible. Based on this experience, a comprehensive kinetic analysis of the electron gas in the cylindrical arrangement of the Franck-Hertz experiment under typical parameter conditions has been performed by using the correspondingly adapted Boltzmann equation for the electrons. A two term approximation of the velocity distribution has been used to elaborate the significant features of the complex electron kinetics.

The study includes an electron accelerating field between a thermionic cathode and a grid and a retarding field between the grid and a partially electron absorbing anode. Closely around the grid a smooth field reversal between the accelerating and retarding regions, with logarithmic potential profiles in each of these, was assumed. Furthermore, in the same spatial range an appropriate electron extraction by the grid was introduced to allow a steady-state flow of electrons between cathode and anode. As far as possible an accurate cross section set of electron collision with mercury atoms has been selected from the literature to describe the elastic collisions and the lowest excitation processes of the electrons in the relevant range of some eV above the respective threshold energies.

Based on a large number of numerical solutions of the resultant kinetic initial-boundary value problem the anode flux characteristics could be deduced in a broad range of the accelerating cathode-grid voltage as well as for different mercury vapour pressures. Furthermore, a spatially resolved analysis of the isotropic and anisotropic part of the electron velocity distribution has been performed to elaborate especially the impact of the elastic collisions on the electron capture in the potential energy valley around the grid and on the formation of the anode flux maxima. This analysis has been extended by a discussion of the spatially resolved representation of the relevant electron transport properties and of the dominant contributions to the electron power balance equation.

Moreover, the overall importance of the various contributions to the energy transfer processes in the electron gas could be elaborated by analysing the balance equation of the spatially integrated energy gain and loss processes per flowing electron between the cathode and the grid position.

Altogether, a detailed picture of the complex kinetics of the electron gas in the cylindrical Franck-Hertz experiment has been presented and some basic assumptions and simplifications used so far in the interpretation of this experiment could be critically evaluated on a sufficiently rigorous kinetic basis.

References

- [1] J. Franck and G. Hertz, *Verh. Deutsche Phys. Ges.* **16**, 457 (1914).
- [2] K. H. Carpenter, *Am. J. Phys.* **43**, 190 (1975).
- [3] W. Buhr, W. Klein, and S. Pressler, *Am. J. Phys.* **51**, 810 (1983).
- [4] D. R. A. McMahon, *Am. J. Phys.* **51**, 1086 (1983).
- [5] F. H. Liu, *Am. J. Phys.* **55**, 366 (1987).
- [6] M. M. Kash and G. C. Shields, *J. Chem. Educ.* **71**, 466 (1994).
- [7] A lot of documents can be found in the web as e.g.
http://www.phy.mtu.edu/~nadgorny/manual_fh.pdf,
<http://web.mit.edu/dward/www/papers/franck-hertz.pdf>.
 A list of further documents is given at
<http://www.hep.fsu.edu/~wahl/phy3802/expinfo/FH.html>.
- [8] W. D. Groot and F. M. Penning, *Anregung von Quantensprünge durch Stoss*, *Handb.d.Phys.* Vol. XXIII (Springer, Berlin, 1933), chap. 2.
- [9] A. C. Melissinos, *Experiments in Modern Physics* (Academic Press, New York, 1966), chap. 1, pp. 8–17.
- [10] G. F. Hanne, *Am. J. Phys.* **56**, 696 (1988).
- [11] R. E. Robson, B. Li, and R. D. White, *J. Phys. B: At. Mol. Opt. Phys.* **33**, 507 (2000).
- [12] R. Winkler, G. Petrov, F. Sigenege, and D. Uhrlandt, *Plasma Sources Sci. Technol.* **6**, 118 (1997).
- [13] R. Winkler, *The Boltzmann equation and transport coefficients of electrons in weakly ionized plasmas*, *Advances in Atomic, Molecular, and Optical Physics* Vol. 43 (Academic, San Diego, 2000), pp. 19–77.
- [14] D. Loffhagen, F. Sigenege, and R. Winkler, in: *Proc. 16. European Conference on Atomic & Molecular Physics of Ionized Gases* Vol. 2, Grenoble, France, 2002, p. 61.
- [15] F. Sigenege and R. Winkler, *Eur. Phys. J. AP* **19**, 211 (2002).
- [16] R. E. Robson, R. Winkler, and F. Sigenege, *Phys. Rev. E* **65**, 056410 (2002).

- [17] G. Petrov and R. Winkler, *Contrib. Plasma Phys.* **37**, 327 (1997).
- [18] J. B. Hasted, *Physics of Atomic Collisions Vol. XXIII* (Butterworths, London, 1964), chap. 3, p. 74.
- [19] J. H. Ingold, *Phys. Rev. E* **56**, 5932 (1997).
- [20] L. L. Alves, G. Gousset, and C. M. Ferreira, *Phys. Rev. E* **55**, 890 (1997).
- [21] R. Winkler and F. Sigenege, *J. Phys. D: Appl. Phys.* **34**, 3407 (2001).
- [22] F. Sigenege and R. Winkler, *Phys. Rev. E* **52**, 3281 (1995).
- [23] F. Sigenege and R. Winkler, *Contrib. Plasma Phys.* **36**, 551 (1996).
- [24] J. P. England and M. T. Elford, *Aust. J. Phys.* **44**, 647 (1991).
- [25] M. Hayashi, *Electron Collision Cross Sections*, in: *Plasma Material Science Handbook* (Tokyo, Ohmsha, 1992), pp. 748.
- [26] N. S. Scott, P. G. Burke, and K. Bartschat, *J. Phys. B: At. Mol. Phys.* **16**, L361 (1983).
- [27] S. Rockwood, *Phys. Rev. A* **8**, 2348 (1973).
- [28] Leybold Didactic GmbH, instruction sheet no. 555 85 (<http://www.leybold-didactic.com>, 1988).
- [29] G. G. Lister and S. E. Coe, *Comp. Phys. Commun.* **75**, 160 (1993).
- [30] V. E. Golant, A. P. Zhilinsky, and I. E. Sakharov, *Fundamentals of Plasma Physics* (New York, Wiley, 1980), p. 72.